buildings

MDPI

Article

Experimental Study on the Seismic Performance of Buckling-Restrained Braces with Different Lengths

Kechuan Wu [1], Guanglan Wei [2,*], Chi Lin [2], Longfei Zhang [1], Wenzheng Yu [1] and Xiang Lan [1]

[1] College of Architecture and Civil Engineering, Kunming University, Kunming 650214, China; wukc@kmu.edu.cn (K.W.); zhanglongfei08052003@kmu.edu.cn (L.Z.); yuwenzheng@kmu.edu.cn (W.Y.); lx523947015@kmu.edu.cn (X.L.)
[2] College of Architecture and Civil Engineering, Dianchi College, Kunming 650228, China; linchi@dcc.edu.cn
* Correspondence: weiguanglan@dcc.edu.cn

Abstract: To investigate the differences in seismic performance of buckling-restrained braces (BRBs) with significantly different lengths and to explore the influence of length on the energy dissipation efficiency of BRBs within the same structure, this study designed and fabricated two BRBs with lengths of 8.5 m and 3 m based on an actual engineering project. Low-cycle reciprocating load tests were conducted to compare the performance of the two BRBs in terms of hysteretic energy dissipation capacity, tension–compression bearing capacity imbalance coefficient, cumulative plastic deformation capacity, and low-cycle fatigue life. Additionally, the energy dissipation and damping efficiency of BRBs of different lengths within the same structure was analyzed. The results indicate that under cyclic loading based on design displacement, the 8.5 m BRB exhibits a greater equivalent viscous damping ratio, cumulative hysteretic energy dissipation, and cumulative plastic deformation, leading to more efficient energy dissipation and damping effects. The length of the brace is a significant factor affecting the imbalance coefficient of tension–compression bearing capacity, with longer braces resulting in a larger imbalance coefficient. The 3 m BRB shows less deviation from the mean values of various fatigue parameters, indicating more stable low-cycle fatigue performance. Within the same structure, shorter BRBs with larger design displacements achieve higher energy dissipation efficiency, allowing for more effective utilization of their energy dissipation capacity. This study's conclusions provide valuable references for designers in the rational selection of BRBs of different lengths in actual engineering projects and offer preliminary insights into the energy dissipation efficiency of BRBs of varying lengths within a structure.

Keywords: buckling-restrained brace; seismic performance; fatigue performance; design displacement; brace length

check for updates

Academic Editor: Hugo Rodrigues

Received: 5 December 2024
Revised: 31 December 2024
Accepted: 2 January 2025
Published: 7 January 2025

Citation: Wu, K.; Wei, G.; Lin, C.; Zhang, L.; Yu, W.; Lan, X. Experimental Study on the Seismic Performance of Buckling-Restrained Braces with Different Lengths. *Buildings* **2025**, *15*, 154. https://doi.org/10.3390/buildings15020154

Copyright: © 2025 by the authors. Licensee MDPI, Basel, Switzerland. This article is an open access article distributed under the terms and conditions of the Creative Commons Attribution (CC BY) license (https://creativecommons.org/licenses/by/4.0/).

1. Introduction

Seismic isolation and energy dissipation technologies represent some of the most effective seismic resistance techniques for buildings, providing means to address earthquake hazards [1]. Moreover, innovative structural components and systems with superior seismic performance are under research and development [2] and are gradually finding their way into practical engineering projects demanding high seismic resilience. Seismic isolation technology primarily involves the installation of isolation pads at a building's foundation to form an isolation layer, thereby preventing transmission of seismic forces to the superstructure and reducing structural seismic response [3]. Energy dissipation technology, on the other hand, involves the installation of energy dissipation devices—such

as buckling-restrained braces (BRBs)—at specific structural locations. These devices absorb or dissipate vibrational energy input by an earthquake, thus controlling structural seismic response [4]. BRBs are one of the most widely used energy dissipation devices, possessing both load-bearing and energy-dissipating functions. They primarily consist of a core energy-dissipating segment and an external restraint segment, as shown in Figure 1a [5]. By preventing buckling, BRBs achieve high compressive load capacity and balanced tensile and compressive strength, with their mechanical performance compared to ordinary braces as shown in Figure 1b [5].

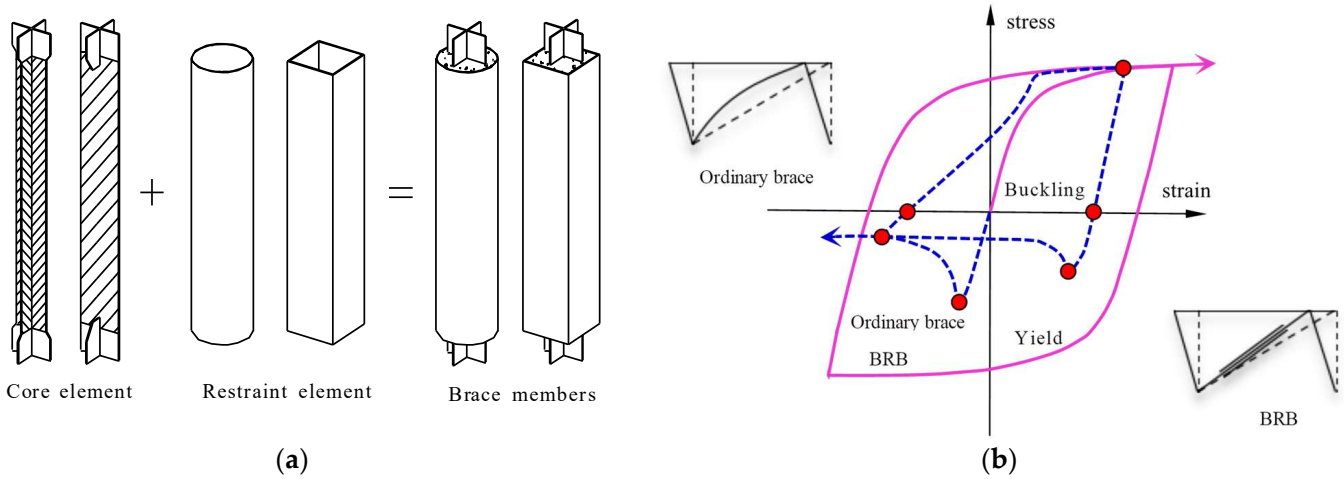


Figure 1. Structure and mechanical performance of buckling-restrained braces: (**a**) composition of buckling-restrained braces; (**b**) comparison of mechanical performance between buckling-restrained braces and conventional braces (The unit of the horizontal axis is %, and the unit of the vertical axis is MPa).

With the official implementation of China's "Regulations on Seismic Management of Construction Projects" (State Order No. 744) on 1 September 2021, the application of BRBs in significant new public buildings and retrofit projects has become increasingly prevalent, particularly in high-seismic-intensity areas. A careful observation of the application characteristics of BRBs in engineering reveals that the use of extra-long BRBs in civil buildings is relatively uncommon. However, with the rising demand for seismic performance in large-span spatial structures and large industrial plant structures in recent years, extra-long BRBs have begun to be gradually applied in these areas. Figure 2 illustrates the application of BRBs with significant length differences in actual projects [6,7]. As the development of large-span spatial structural systems progresses, the application of extra-long BRBs will become more widespread. Nonetheless, there is currently limited comparative research on the mechanical performance of BRBs with significant length differences, and studies on the differences in energy dissipation and seismic reduction effects of BRBs with significant length variations within the same structure are rare. These two aspects are the main focus of the research in this paper.

The seismic performance of BRBs is generally related to factors such as their yield bearing capacity, the restraining ratio (the ratio of the stable bearing capacity of the restraining member to the yield bearing capacity of the core segment), unbonded materials, the yield strength of the core material, and the length of the braces.



Figure 2. Application of BRBs in different structural systems: (**a**) short BRBs; (**b**) long BRBs.

In a study on the impact of brace length on performance, Pandikkadavath et al. [8] employed a combined approach of finite element analysis and theoretical derivation to investigate the hysteretic energy dissipation capacity of BRBs with different yield segment lengths. They also applied BRBs with short yield segments to the seismic performance evaluation of frame structures. The results showed that BRBs with short yield segments possess stable hysteretic energy dissipation capability. The elastic stiffness and post-yield stiffness increase as the yield segment length of the BRB decreases, while energy dissipation capacity decreases. The yield segment length has no significant effect on the strength adjustment factor. Additionally, BRBs with short yield segments can effectively reduce inter-story displacement and residual displacement responses in low-rise building frames. Sahoo et al. [9] designed and fabricated three BRB specimens with a yield segment length of 300 mm and conducted quasi-static tests to investigate their overall stability, hysteresis curve characteristics, strength adjustment factor, energy dissipation capacity, and equivalent viscous damping coefficient. The results indicated that at a loading strain of 4.2%, the average equivalent viscous damping coefficient of the three specimens was 43.5%, demonstrating good energy dissipation performance. At a 5% loading strain, the maximum strength adjustment factor for the specimens was 1.15, which was similar to that of conventional-length BRBs. Gao C X et al. [10] also studied the impact of yield segment length on the hysteretic performance of BRBs. They found that BRBs with short yield segments enter the plastic energy dissipation stage earlier, with higher strain levels and better energy dissipation efficiency, but poorer low-cycle fatigue performance, which may lead to premature failure. Moreover, by comparing the skeleton curves of BRBs with different lengths, they observed that the yield displacement of BRBs is proportional to the yield segment length and inversely proportional to the brace stiffness. Reducing the yield segment length results in a decrease in both the elastic stiffness and post-yield stiffness of the brace. Sitler et al. [11] used numerical simulations to study the development of higher-order buckling modes and corresponding friction effects in ultra-long BRBs. They established two-dimensional shell and three-dimensional solid models using Abaqus to investigate the impact of parameters such as the core segment yield length, higher-order mode buckling wavelength, and steel grade on the performance of BRBs. The results showed that the strength adjustment factor is related to the friction coefficient, debonding gap ratio, yield segment length, and width-to-thickness ratio, and the steel grade also affects the strength adjustment factor. The proposed method for calculating the strength adjustment factor, as well as the formulas for the debonding gap and design strain, is of great significance for the design and performance evaluation of ultra-long BRBs. These methods help in

understanding the mechanical performance of ultra-long BRBs and provide theoretical guidance and methods for the design of such products, which can reduce experimental costs and improve the reliability of product designs. Mirtaheri et al. [12] conducted cyclic loading tests on BRBs with the same yield capacity but different energy dissipation segment lengths. The results showed that as the length of the energy dissipation segment decreases, the low-cycle fatigue performance of BRBs gradually declines, reflecting the detrimental effect of uneven strain distribution on fatigue performance.

The above study focuses on various seismic performance indicators of BRBs with short yielding segments and preliminarily explores the influence of yielding segment length on BRB performance. It compares and analyzes the performance differences of BRBs with different yielding segment lengths. However, the few existing studies on the seismic performance of ultra-long BRBs have not yet conducted comparisons with the performance of short BRBs.

In recent years, the study of dual-stage yielding BRBs based on the combination of long and short energy-dissipating segments, as well as those based on multiple energy dissipation mechanisms, has become a research focus among many scholars. Kazemi F et al. [13] developed a novel dual-stage yielding steel slit damper–buckling-restrained brace (SSD-DYB) system, primarily aimed at enhancing the seismic performance of steel structures. The research found that the U-shaped elements in the damper system exhibit excellent seismic resilience under seismic loads, which is of significant importance for the seismic retrofitting of old buildings. Additionally, the study discovered that altering the number and shape of the steel slit damper strips significantly affects the maximum load and area of the hysteresis curve, offering good adaptability for controlling specific performance targets of buildings. An optimized SSD-DYB system was proposed to enhance the seismic performance of both new and retrofitted structures. Xiong C et al. [14] proposed a replaceable core segment dual-stage yielding BRB in series with long and short energy-dissipating core segments. The first stage of yielding is achieved through the short energy-dissipating core segment, while the second stage relies on the long energy-dissipating core segment. Essentially, it utilizes the energy dissipation efficiency differences of BRBs of different lengths under the same deformation to achieve staged yielding of the core energy-dissipating segment. The hysteresis performance, failure modes, and cumulative plastic deformation capacity of this dual-stage yielding BRB were studied through quasi-static tests. Sun J et al. [15], based on a similar concept, proposed a dual-stage yielding BRB with displacement-triggering functionality featuring long and short energy-dissipating core segments in series. The core idea is that the deformation of the damper initially concentrates on the short energy-dissipating core segment. Once the displacement limit is triggered, the deformation is transferred to the long energy-dissipating core segment, effectively achieving the dual-stage yielding function. Wu C et al. [16] proposed a dual-stage yielding BRB composed of multiple energy-dissipating segments with different cross-sectional areas and lengths in parallel. Due to the premature yielding of the short core energy-dissipating segment, the dual-stage BRB exhibits a smaller yield displacement and a larger equivalent viscous damping ratio at small deformations compared to single-stage BRBs of the same model.

In comparison to the aforementioned studies, this paper focuses on the performance differences of BRBs with significantly varying lengths. It analyzes the energy dissipation efficiency issues of BRBs with notable length differences within the same structure. The research findings are expected to provide further insights for the product design of dual-yield BRBs.

In the study of the influence of other parameters on the performance of braces, Guo Y L et al. [17] found that the value of the constraint ratio significantly affects the energy

dissipation capacity of a buckling-restrained brace (BRB). They indicated that when the constraint ratio is sufficiently high, an appropriately sized gap (the gap between the core segment and the restraining component) can enable full energy dissipation of the BRB; however, an excessively large gap will reduce its seismic performance. Zhou Y et al. [18] conducted low-cycle reversed load tests on five prefabricated all-steel buckling-restrained braces, investigating the effects of non-bonded materials, constraint ratios, and loading regimes on the mechanical properties of BRBs. Based on the design principle that the BRB should yield before the main structure and avoid premature failure due to insufficient plastic deformation capacity, they proposed that the cumulative plastic deformation coefficient of the BRB should not be less than 1200. Jia M M et al. [19] examined the differences in energy dissipation capacities of buckling-restrained braces under various loading regimes and constraint ratios, pointing out that the magnitude of multi-wave buckling deformation is a key factor affecting the fatigue performance of BRBs. Lu J K et al. [20] conducted experimental research on buckling-restrained braces with varying-thickness steel plates, revealing that the incorporation of stiffening ribs in the BRB reduces wear of the non-bonded material at the ends of the variable-thickness core and effectively enhances the low-cycle fatigue performance of the variable-thickness core BRB. Wu A J et al. [21] performed cyclic load tests and finite element analyses on all-steel BRBs under different loading modes, studying the development process and mechanisms of multi-wave buckling deformation in BRBs, and found significant differences in the buckling wavelength and fatigue life of BRBs under various loading modes. Fujita et al. [22] investigated the impact of gap values on the hysteretic performance and failure modes of BRBs, proposing construction techniques for the precise control of gap values. The results indicated that as the gap value increases, the energy dissipation capacity of the BRB gradually decreases, the failure mode transitions from tensile fracture to local buckling failure, and the failure location shifts from the middle section toward the ends.

The above research primarily focuses on the effects of factors such as the constraint ratio, loading protocol, loading pattern, and gap value on the seismic performance of BRBs. There is little research concerning the energy dissipation efficiency of BRBs and its influencing factors.

In summary, there is currently limited research on the impact of brace length on the seismic performance of BRBs. Among the few studies focusing on the seismic performance of ultra-long BRBs, comparative analyses with shorter BRBs have not yet been conducted. Additionally, there is a scarcity of research on the energy dissipation efficiency of BRBs and its influencing factors. Based on this, the present study designed and fabricated two BRBs with lengths of 8.5 m and 3 m, respectively, for a specific engineering project. Through low-cycle reciprocating load tests, this study investigates the impact of brace length on various performance indicators, such as energy dissipation capacity, tension–compression strength imbalance coefficient, cumulative plastic deformation capacity, and low-cycle fatigue life. Furthermore, it compares and analyzes the energy dissipation and damping efficiency of BRBs with significantly different lengths within the same structure. The research findings are expected to provide valuable references for the rational selection of BRBs of different lengths in practical engineering and to offer preliminary insights into the energy dissipation and damping efficiency of BRBs of varying lengths within structures. Based on the research background and discussion, the technical roadmap of this study was formulated, as shown in Figure 3.

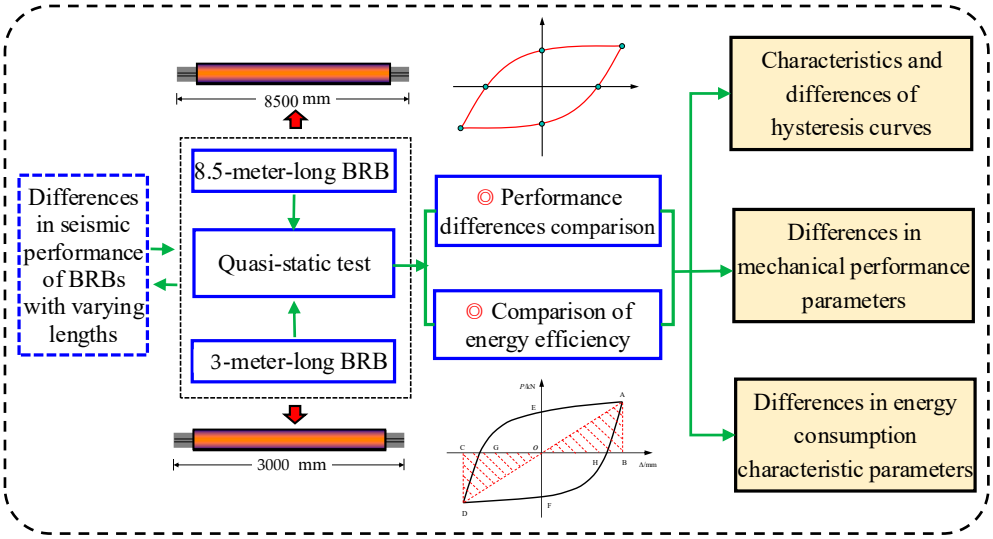


Figure 3. The technical roadmap of the thesis.

2. Experimental Overview

2.1. Specimen Design

Two BRBs were designed and fabricated with lengths of 8.5 m and 3 m, designated as BRB-L and BRB-S, respectively. The braces consist of an energy-dissipating core segment and an external restraining segment. The core segment has a rectangular "line-shaped" cross-section, and the external restraining segment is a concrete-filled steel tube. A 1.5 mm unbonded layer, made of polyethylene sheets, is placed between the concrete and the core segment. Both the core and restraining segment materials of the specimens are made from Q235-B steel. The main dimensions and planar configurations of the specimens are shown in Figure 4. The energy-dissipating core segment of the BRBs is cut from a single steel plate, with stiffening ribs in the connection segment welded to form an integral part with the core segment. To prevent the restraining tube from sliding, a positioning clip is set at the midpoint along the axial direction of the core segment. The unbonded material is adhered to the entire surface of the core segment covered by the restraining segment. Once positioned, the core segment is placed inside the restraining tube, followed by the pouring of concrete fill and the curing of the specimen. During the BRB design, the cross-sectional area A_c of the core segment is calculated using Equation (1), and the cross-sectional area A_l of the elastic connection segment is calculated using Equation (2) to ensure that the connection segment remains elastic. To ensure the overall stability of the BRB, the restraining ratio ζ (defined as the ratio of the elastic buckling capacity F_{cr} of the external restraining segment to the yield capacity F_y of the BRB) must satisfy the requirements of Equation (3). To ensure local stability, the wall thickness t_r of the external restraining steel tube and the strength f_c of the concrete fill must satisfy the requirements of Equation (5). Detailed design parameters for each component of the specimens BRB-L and BRB-S, designed according to the above method, are provided in Table 1.

$$F_y = f_y A_c \tag{1}$$

$$F_c = f_y A_l \geq 1.2\omega F_y \tag{2}$$

$$\zeta = \frac{F_{cr}}{F_y} \geq 1.95 \tag{3}$$

$$F_{cr} = \frac{\pi^2 (E_c I_c + E_s I_s)}{l_r} \tag{4}$$

$$t_r \geq \frac{f_{ck} b_c}{12 f} \tag{5}$$

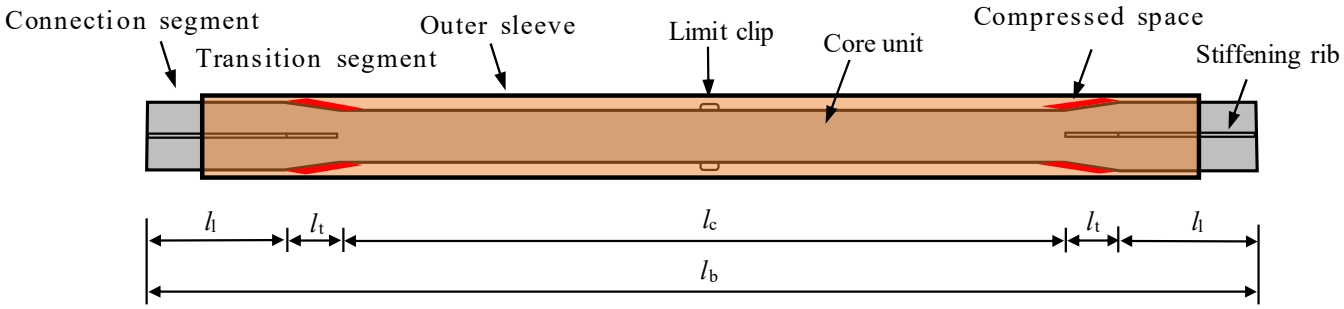


Figure 4. The geometric dimension diagram of the BRB appearance.

Table 1. Dimension parameters of BRBs.

Specimen Number	Total Length of Brace l_b/mm	Internal Structural Composition							Gap c/mm	Peripheral Constraint Segment		
		Energy Dissipation Segment				Transition Segment	Connection Segment			Steel Casing		Concrete
		l_c/mm	b_c/mm	t_c/mm	A_c/mm^2	l_t/mm	l_l/mm	A_l/mm^2		t_r/mm	l_r/mm	f_c/MPa
BRB-L	8500	6110	55	10	550	425	770	1660	1.5	6	8200	11.9
BRB-S	3000	1648	55	10	550	150	526	1660	1.5	2	2700	11.9

Note: A_c and A_l represent the cross-sectional areas of the energy-dissipating segment and the connecting segment, respectively. l_c, l_t, l_l, and l_r denote the lengths of the energy-dissipating segment, transition segment, connecting segment, and constrained casing, respectively. b_c and t_c refer to the width and thickness of the energy-dissipating segment, while t_r indicates the wall thickness of the constrained steel casing. f_c represents the compressive strength of the concrete within the constrained casing.

In the formula, F_y represents the yield bearing capacity of the BRB, f_y is the measured yield strength of the steel, and ω is the strain hardening adjustment coefficient for the steel, which can be taken as 1.5 for Q235 steel. E_s and E_c are the elastic moduli of the steel casing and the filled concrete, respectively. I_s and I_c are the moments of inertia for the steel casing and the filled concrete, respectively. f_{ck} is the standard value of compressive strength for the concrete filled within the casing, b_c is the width of the core segment of the BRB, and f is the design value of the steel strength.

2.2. Material Property Test

To accurately understand the mechanical properties of the steel used for the fabrication of BRB specimens, and to facilitate the precise design of the BRB test specimens, uniaxial tensile tests were conducted on Q235 steel from the same batch used for this experiment. The tests were carried out in accordance with the requirements of GB/T 288.1-2010 "Method of Tensile Testing of Metallic Materials at Room Temperature" [23]. The tensile tests were performed on a 100 kN universal testing machine. The tensile samples were taken from steel plates of the same batch and identical thickness. The dimensions of the samples and the tensile stress–strain curve of the material are shown in Figure 5, with the results of the material property tests provided in Table 2.

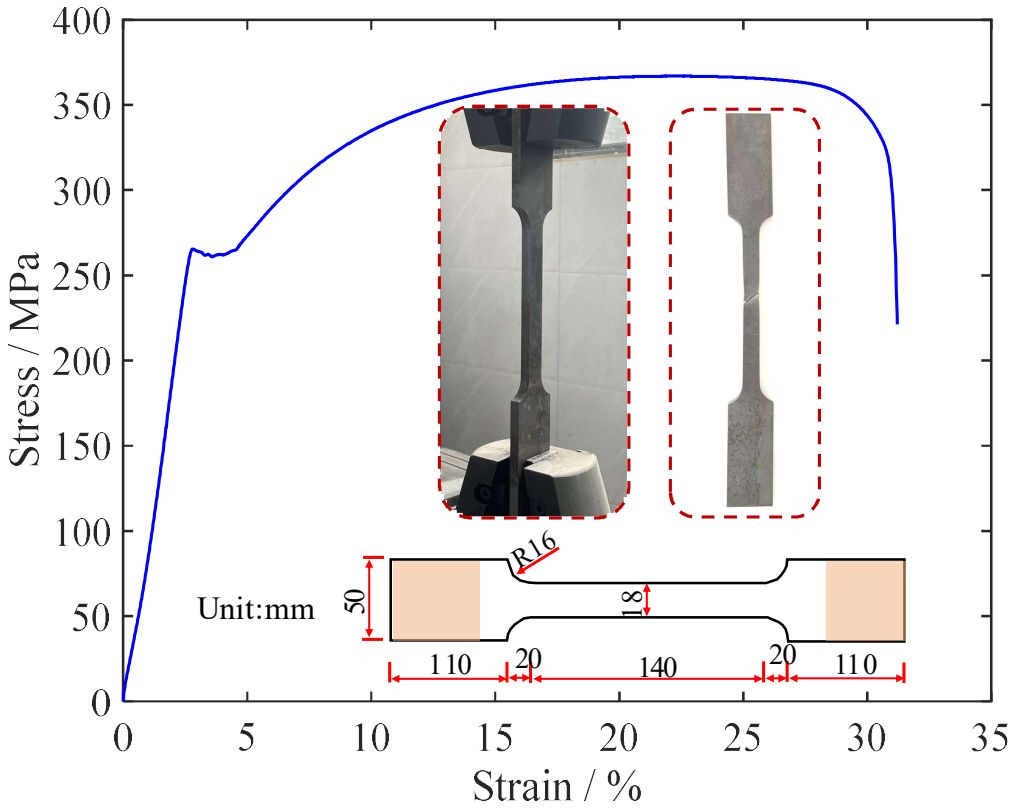


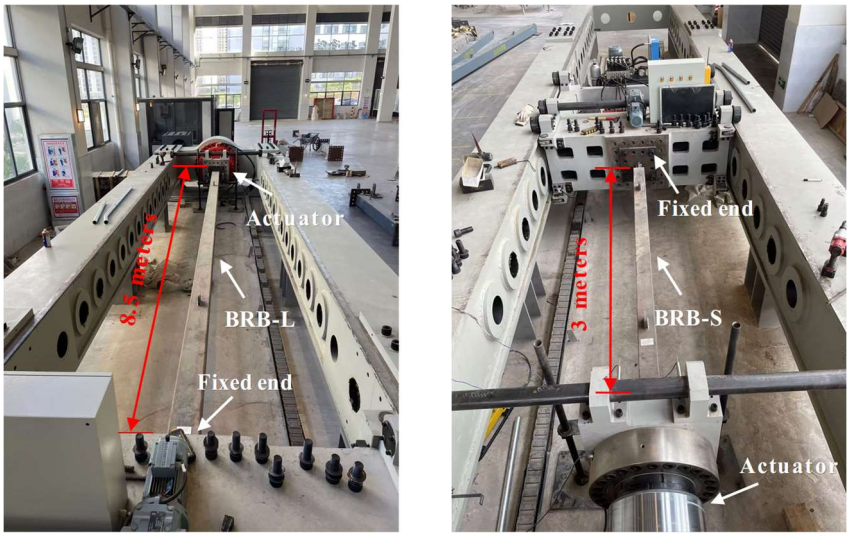
Figure 5. Tensile stress–strain relationship for Q235.

Table 2. Material properties.

Material	Yield Strength f_y/MPa	Tensile Strength f_u/MPa	Elastic Modulus E_s/GPa	Elongation Rate A/%
Q235	269	371	209.45	31.52

2.3. Experimental Loading and Measurement Scheme

The experimental loading setup is shown in Figure 6. The maximum tensile and compressive capacity of the loading equipment is 8000 kN, with a displacement stroke of ±500 mm. Following the requirements for BRB performance testing outlined in the DBJ 53/T-125-2021 [24] "Technical Regulations for Application of Energy Dissipation and Seismic Mitigation in Buildings" of Yunnan Province, China, a force–displacement hybrid control mode was used for loading. Prior to the yielding of the specimen, cyclic loading was conducted three times at a load amplitude of $0.5F_y$, where F_y is the design yield load capacity of the BRB. After yielding, based on the design displacement Δ_b of the BRB (Δ_b represents the deformation value of the corresponding BRB in the actual structure under rare seismic events), cyclic loading was performed three times at displacement amplitudes of $0.5\Delta_b$, $0.8\Delta_b$, $1.0\Delta_b$, and $1.2\Delta_b$. Additionally, cyclic loading was conducted 60 times at a displacement amplitude of $1.0\Delta_b$ to verify the low-cycle fatigue performance of the BRB. Detailed information on the experimental loading scheme is provided in Table 3, and the loading protocol is illustrated in Figure 7. In actual engineering projects, the yield load capacity F_y for both BRB-L and BRB-S is 150 kN, with design displacements Δ_b of 16 mm and 12 mm, respectively.



(**a**) (**b**)

Figure 6. Test loading site photo: (**a**) BRB-L loading site; (**b**) BRB-S loading site.

Table 3. Experimental loading scheme details.

Load Control Mode	Loading Level	Load Amplitude F/F_y	The Number of Cycles/n
Force control	1	0.5	3
	Loading level	**Displacement amplitudeΔ/Δ_b**	**The number of cycles/n**
Displacement control	2	0.5	3
	3	0.8	3
	4	1.0	3
	5	1.2	3
	6	1.0	60

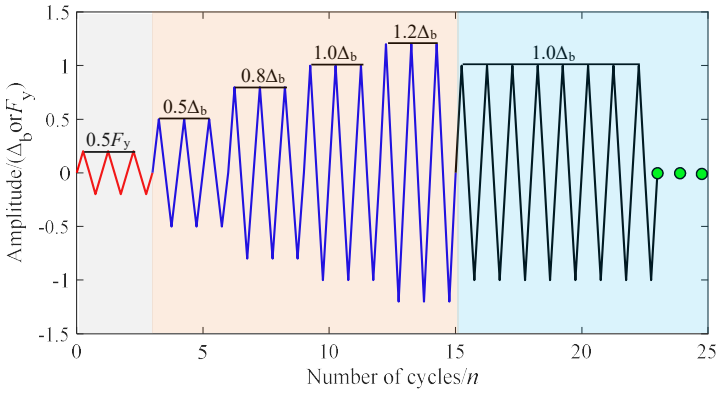
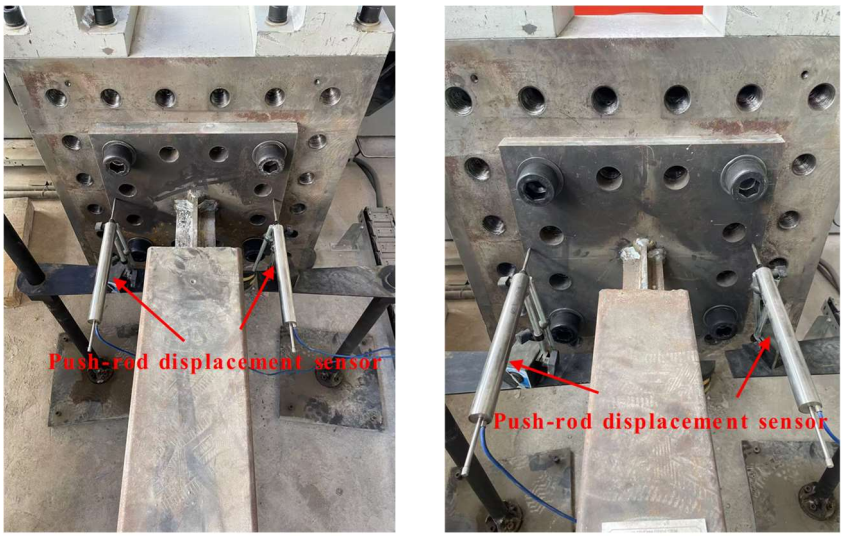


Figure 7. Diagram of the loading system.

The experiment primarily measured the axial load on the buckling-restrained brace (BRB) and the relative displacement at both ends of the brace. The axial load was obtained through a force sensor on the actuator, and the displacement was measured using a plunger-type displacement gauge. Two displacement gauges were positioned on the left and right sides of the BRB, and the average of the data collected by these two gauges was taken as the axial deformation value of the BRB, as shown in Figure 8.



(**a**) (**b**)

Figure 8. Displacement sensor arrangement: (**a**) BRB-L displacement sensor arrangement; (**b**) BRB-S displacement sensor arrangement.

3. Experimental Results and Analysis

3.1. Hysteresis Curves and Characteristic Analysis

The load–displacement hysteresis curves of specimens BRB-L and BRB-S are shown in Figure 9, where compression is positive, tension is negative, F represents the axial load of the BRB, and Δ represents the axial deformation of the BRB. From the figure, it can be observed that the hysteresis curve of specimen BRB-L is less full compared to that of specimen BRB-S, mainly reflected in the size difference of the hysteresis curve contours, which indicates the corresponding hysteresis energy dissipation capacity. The difference in the area of the hysteresis curves between the second and fourth quadrants is particularly noticeable, with specimen BRB-S exhibiting stronger energy dissipation capacity under various load levels, as indicated by the larger area of each loop's hysteresis curve under each load level. This result can also be easily compared by observing the shaded areas of the hysteresis curves under various load levels in Figure 9. The analysis reveals that the length of specimen BRB-L is 2.83 times that of specimen BRB-S, but in the actual structure, the design displacement of BRB-L is only 1.33 times that of BRB-S. In the same structure, specimen BRB-L has a larger yield displacement and a smaller design working displacement, while specimen BRB-S has a smaller yield displacement and a larger design working displacement. The ductility deformation ratios (the ratio of BRB design working displacement to yield displacement) for the two specimens are 1.39 and 3.91, respectively, differing by about 2.8 times. Therefore, the hysteresis curve of specimen BRB-S is more full. This also indicates that the energy dissipation efficiency of BRBs with different lengths in the same structure can be qualitatively assessed using the ductility deformation ratio as an indicator. Overall, the hysteresis curves of specimens BRB-L and BRB-S exhibit good symmetry and are spindle-shaped, with neither specimen experiencing overall or local instability failure throughout the test. However, it was noted that from the second loading stage onwards, the area of the first loop's hysteresis curve in each loading stage of specimen BRB-L is slightly larger than the other two loops, as detailed in Table 4. This is primarily because the displacement amplitude in each loading stage of specimen BRB-L is relatively small, resulting in relatively minor plastic deformation from the second to the last loading stage, indicating a lighter degree of plasticity. Therefore, a more pronounced Bauschinger effect is present, meaning the load when entering yield in

the first loop is slightly greater than in the other two loops [25,26]. This also suggests that the hysteresis energy dissipation capacity of the brace has not been fully utilized, possibly due to conservative design during the BRB product development. In contrast, the hysteresis curves of specimen BRB-S in each loading stage are nearly coincident, indicating stable hysteresis energy dissipation capacity of the BRB, with no apparent strength or stiffness degradation, demonstrating good energy dissipation capability. The blue dashed line in Figure 9 represents the backbone curve formed by connecting the origin with the peak load points after yielding under tension and compression. Kazemi F et al. [13] pointed out that the backbone curve is primarily used to describe the maximum load capacity of the damper under increasing displacement, representing the idealized performance of the damper. It clearly expresses the characteristics of the damper's elasticity, yielding, strain hardening, and gradual stabilization and can be used to establish a theoretical recovery force model for the damper, serving as an important characteristic curve for expressing the mechanical performance of the damper. It is easy to see from Figure 9 that both specimens exhibit a clear yield inflection point on their backbone curves, and after yielding, they continue to show a stable increase in strength, with a significant strain hardening effect, indicating that the plastic deformation capacity and hysteresis energy dissipation capacity of both specimens have not shown any signs of decline.

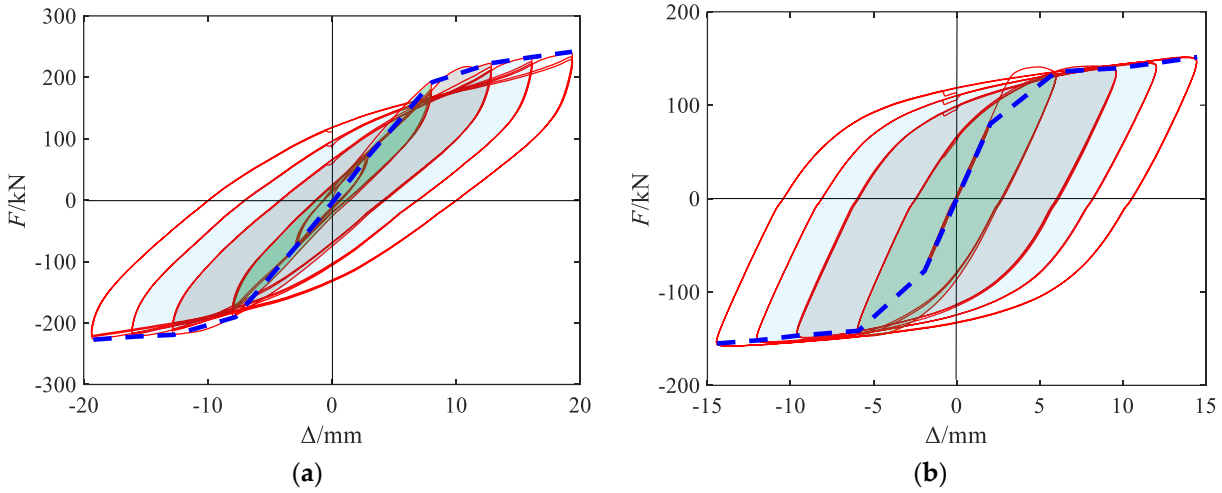


Figure 9. Load–displacement hysteresis curves of BRB: (**a**) BRB-L; (**b**) BRB-S.

Table 4. Energy dissipation values at various loading displacement amplitudes for BRB (kN·mm).

Sample Number	Amplitude of Load Displacement											
	$0.5\Delta_b$			$0.8\Delta_b$			$1.0\Delta_b$			$1.2\Delta_b$		
	First Cycle	Second Cycle	Third Cycle	First Cycle	Second Cycle	Third Cycle	First Cycle	Second Cycle	Third Cycle	First Cycle	Second Cycle	Third Cycle
BRB-L	855	694	642	2819	2758	2657	4628	4642	4566	6798	6787	6710
BRB-S	1160	1152	1125	2837	2823	2807	4124	4043	4029	5448	5385	5384

Table 4 presents the energy dissipation values for specimens BRB-L and BRB-S at various displacement amplitudes during the displacement-controlled loading phase. The energy dissipation of the BRBs corresponds to the area of the respective hysteresis loops. From Table 4, it can be observed that the area of each hysteresis loop for specimens BRB-L and BRB-S increases with the increase in loading displacement, indicating that the energy dissipated by both specimens also increases, demonstrating good hysteretic energy dissipation capacity. At displacement amplitudes of $0.5\Delta_b$, $0.8\Delta_b$, $1.0\Delta_b$, and $1.2\Delta_b$, the

energy dissipated by specimen BRB-S is 1.57 times, 1.03 times, 0.88 times, and 0.80 times that of specimen BRB-L, respectively.

3.2. Skeleton Curves and Characteristic Analysis

Figure 10 illustrates the skeleton curves extracted from the load–displacement hysteresis curves of specimens BRB-L and BRB-S. From the figure, it can be observed that the skeleton curves of both specimens exhibit a distinct bilinear characteristic, indicating that a bilinear model can be employed in finite element analysis to simulate their hysteretic mechanical behavior. Additionally, it is evident that the yield load of each specimen under compression is slightly higher than under tension. This is attributed to the Poisson's effect of the steel under compression and the friction effect between the core segment and the restraint segment. The post-yield stiffness values of specimens BRB-L and BRB-S on the compression side are 2.89 kN/mm and 1.47 kN/mm, respectively, while on the tension side, they are 1.33 kN/mm and 1.59 kN/mm, respectively. Analyzing these data reveals that the post-yield stiffness of specimen BRB-S on the compression side is quite close to that on the tension side, whereas for specimen BRB-L, the post-yield stiffness on the compression side is significantly greater than that on the tension side, and the difference in post-yield stiffness on the tension side between the two specimens is not substantial. The energy-dissipating core segment of the BRB undergoes high-order multi-wave buckling deformation under compression. These buckling deformations make contact with the restraint segment at the wave peaks and troughs, generating a normal compressive force that induces tangential friction effects. The greater the number of buckling waves generated when the BRB is under compression, the larger the corresponding frictional force, which manifests as an increase in the axial compressive load-bearing capacity of the BRB, thereby contributing to its stiffness under compression. Existing research findings suggest that the number of buckling waves generated by a BRB under the same axial compressive load is positively correlated with its length, meaning the longer the BRB, the more buckling waves are produced [27]. This explains why the post-yield stiffness of specimen BRB-L on the compression side is significantly greater than that on the tension side, whereas for specimen BRB-S, the post-yield stiffness on the compression side is closer to that on the tension side. This analysis also indirectly indicates that the tensile and compressive characteristics of ultra-long BRBs are not entirely consistent, particularly for the performance changes under compression, which are closely related to their length. These changes and features warrant additional attention in the design and engineering application of ultra-long BRB products, as they may adversely affect the structure.

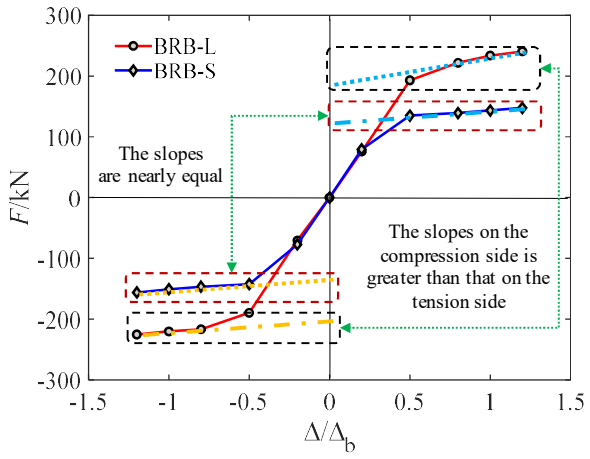


Figure 10. Skeleton curve of BRBs.

3.3. Tension–Compression Capacity Imbalance Coefficient

The difference in peak loads during the tension and compression loading processes of BRB is represented by the tension–compression capacity imbalance coefficient, β. This coefficient is defined as the ratio of the maximum compressive load (P_{cmax}) to the maximum tensile load (P_{tmax}) in the i-th cycle of the BRB load–displacement hysteresis curve, i.e., $\beta = P_{cmax}/P_{tmax}$. The tension–compression capacity imbalance coefficient primarily reflects the impact of friction effects between the energy-dissipating segment and the restraining segment on the asymmetry of tension and compression capacity. According to the American ANSI/AISC 341-16 [28] standard, the coefficient β should not exceed 1.5, and the Chinese JGJ 99-2015 [29] "Technical Specification for Steel Structures of Tall Buildings" stipulates that β should not exceed 1.3. Figure 11 illustrates the distribution of the tension–compression capacity imbalance coefficient β for specimens BRB-L and BRB-S under the first five levels of cyclic loading. It is evident from the figure that the tension–compression capacity imbalance coefficients for both specimens meet the requirements of ANSI/AISC 341-16 and JGJ 99-2015. The maximum values of the tension–compression capacity imbalance coefficient for specimens BRB-L and BRB-S under various cyclic loads are 1.068 and 1.003, respectively. The results indicate that the implemented unbonded layer effectively controls the friction effect between the BRB energy dissipation segment and the restraining segment. It is also noted that with an increase in the number of cyclic loadings, the tension–compression capacity imbalance coefficient of specimen BRB-L gradually becomes greater than that of specimen BRB-S. This is mainly because the core energy-dissipating segment of specimen BRB-L is significantly longer than that of specimen BRB-S. Consequently, under axial loading, BRB-L generates a greater number of higher-order multi-wave buckling, which induces normal local compressive forces on the restraining segment at the peaks and troughs of the waves, thereby generating frictional forces between the energy-dissipating and restraining segment. The greater the number of buckling waves generated by the BRB under axial loading, the greater the frictional force between the energy-dissipating and restraining segment, leading to a larger corresponding tension–compression capacity imbalance coefficient. It is noteworthy that the magnitude of the tension–compression imbalance coefficient significantly influences the safety and design of the BRB connection joints.

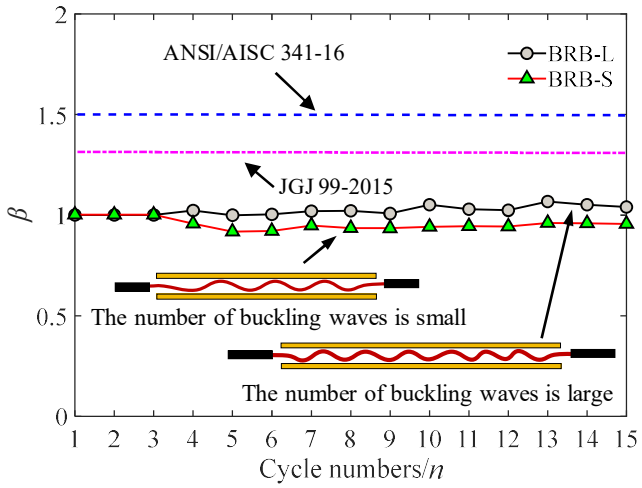


Figure 11. Distribution of the tensile and compressive bearing capacity imbalance coefficient.

3.4. Equivalent Viscous Damping Ratio

Buckling-restrained braces are classified as displacement-type energy dissipation devices, and their energy dissipation capacity can be represented by the equivalent viscous damping ratio. Considering the tension–compression asymmetry of the hysteresis curves

for each specimen, calculations are performed separately for the positive loading (compression) and negative loading (tension) hysteresis curves. The calculation formulas can be found in references [30,31] as shown in Equations (6) and (7), with a schematic diagram of the calculation presented in Figure 12.

$$\zeta_{eq}^{+} = \frac{1}{2\pi}\frac{S_{AGH}}{S_{OAB}} \tag{6}$$

$$\zeta_{eq}^{-} = \frac{1}{2\pi}\frac{S_{DGH}}{S_{OCD}} \tag{7}$$

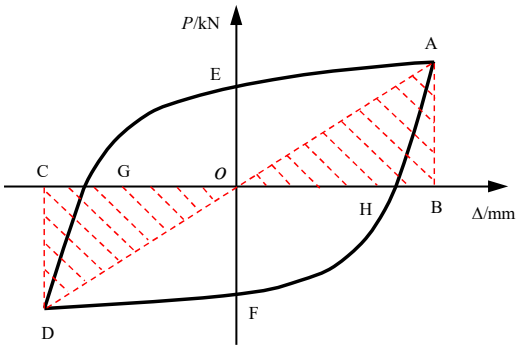


Figure 12. Illustration of the calculation of equivalent viscous damping ratio.

In the formula, S_{OAB} and S_{OCD} represent the areas of the shaded triangles in Figure 12, while S_{AGH} and S_{DGH} denote the areas of the upper and lower halves of the hysteresis loop in Figure 12.

Using the aforementioned method, the equivalent viscous damping ratios for the two specimens under forward loading displacement amplitudes from level 2 to level 5, and under reverse loading displacement amplitudes, are shown in Figure 13. The equivalent viscous damping ratios to the right of the red dashed line in the figure are calculated using Formula (6), while those to the left are calculated using Formula (7). It can be observed from the figure that the equivalent viscous damping ratio of specimens BRB-L and BRB-S increases with the axial loading displacement amplitude, reaching maximum values of 26% and 39.3%, respectively. This indicates that within the same structure, the longer BRB contributes less to the energy dissipation capability of the structure, meaning that the energy dissipation potential of the longer BRB is not fully realized. Overall, the equivalent viscous damping ratios of specimens BRB-L and BRB-S maintain a positive growth trend.

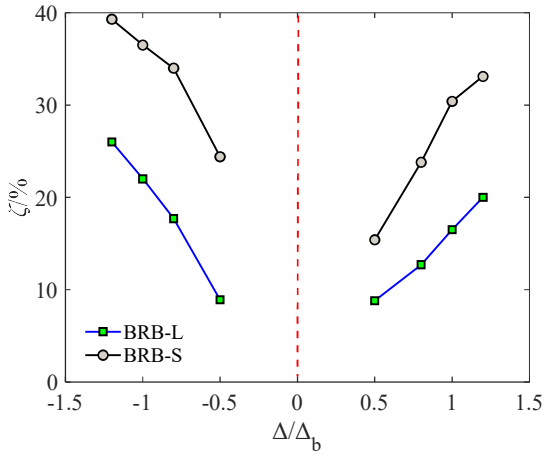


Figure 13. Equivalent viscous damping ratio.

3.5. Equivalent Stiffness

Figure 14 illustrates the relationship between the measured secant stiffness (equivalent stiffness) of specimens BRB-L and BRB-S and the loading displacement. Due to the asymmetric tensile and compressive bearing capacity of BRBs [32], the secant stiffness was calculated separately for tension and compression. The secant stiffness was determined according to the calculation methods outlined in JGJ/T 101-2015 [33] "Technical Specification for Seismic Test of Buildings", specifically using Formulas (8) and (9). As observed in Figure 14, both specimens BRB-L and BRB-S exhibit a well-defined stiffness degradation pattern. At smaller loading displacement amplitudes, the stiffness decreases rapidly; however, as the loading displacement increases, the rate of decline in secant stiffness becomes more gradual. Furthermore, the degree of stiffness degradation in BRB-S is significantly greater than that in BRB-L. This indirectly suggests that in the same structure, the energy dissipation capacity of longer BRBs is more limited.

$$K_s^+ = \frac{F_i^+}{\Delta_i^+ - \Delta_0} \tag{8}$$

$$K_s^- = \frac{F_i^-}{\Delta_i^- - \Delta_0} \tag{9}$$

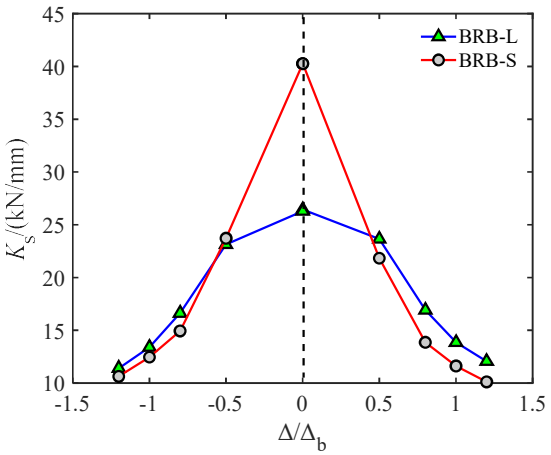


Figure 14. Stiffness degradation curve.

In the formula, F_i^+ and F_i^- represent the compressive and tensile axial loads at the displacement amplitudes during the *i*-th cycle on the hysteresis curve, respectively. Δ_i^+ and Δ_i^- correspond to the displacement amplitudes of compressive and tensile loads F_i^+ and F_i^- during the *i*-th cycle on the hysteresis curve. Δ_0 is the median of the compressive and tensile displacements when the axial load is zero under the same cyclic loading.

3.6. Cyclic Strengthening Coefficient

The cyclic strengthening effect of each specimen is characterized using the cyclic strengthening coefficient, ψ, which is defined as the ratio of the maximum tensile and compressive loads on the hysteresis curves of subsequent cycles to the maximum tensile and compressive loads on the first cycle's hysteresis curve. Figure 15 illustrates the relationship between the cyclic strengthening coefficient values and the number of loading cycles for specimens BRB-L and BRB-S. It can be observed that under tensile and compressive cyclic loading, the cyclic strengthening coefficient values for specimens BRB-L and BRB-S range from 0.91 to 1.25 and 0.93 to 1.19, as well as 0.94 to 1.08 and 0.98 to 1.07, respectively. The symmetry of the tensile and compressive cyclic strengthening coefficients across the

specimens is relatively consistent, indicating that BRBs exhibit similar and stable mechanical properties under both tensile and compressive loading conditions.

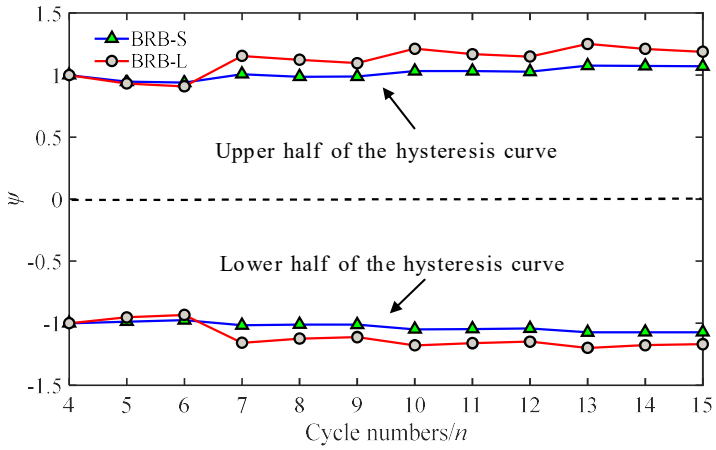


Figure 15. Trend of variation in the cyclic strengthening coefficient.

3.7. Cumulative Plastic Deformation Coefficient and Cumulative Hysteretic Energy Dissipation Coefficient

The cumulative plastic deformation coefficient (*CPD*) and the cumulative hysteretic energy dissipation coefficient (*CPE*) are important indicators for evaluating the performance of BRBs. The formula for calculating the cumulative plastic deformation capacity *CPD* can be found in reference [34], and the formula for the cumulative hysteretic energy dissipation coefficient *CPE* can be found in reference [35], as shown in Equations (10) and (11).

$$CPD = \sum_{i=1}^{n} \left[2\left(\left|\Delta^{+}_{\max}\right| + \left|\Delta^{-}_{\max}\right|\right)/\Delta_{\mathrm{by}} - 4\right] \tag{10}$$

$$CPE = \frac{\int F d\Delta}{2 \times \dfrac{F_{\mathrm{y}}\Delta_{\mathrm{by}}}{2}} = \frac{\int F d\Delta}{F_{\mathrm{y}}\Delta_{\mathrm{by}}} \tag{11}$$

In the formula, $\Delta^{+}{}_{\max}$ and $\Delta^{-}{}_{\max}$ represent the maximum compressive and tensile displacements of the buckling-restrained brace (BRB) during the i-th cycle of loading, respectively, and n is the number of loading cycles. F denotes the load magnitude on the BRB during cyclic loading, Δ is the corresponding BRB displacement, and Δ_{by} is the yield displacement of the BRB.

The coefficient *CPD* primarily reflects the cumulative plastic deformation capacity of a BRB under cyclic loading, while the coefficient *CPE* mainly indicates the ability of a BRB to accumulate dissipated input energy. The *CPD* values for specimens BRB-S and BRB-L, calculated using Formula (10), are 2146 and 1891, respectively, both meeting the ANSI/AISC 341-16 standard requirement of not less than 200. Figure 16 shows the single-cycle energy dissipation coefficient and cumulative energy dissipation coefficient for specimens BRB-L and BRB-S, calculated using Formula (11). It is evident that for both specimens, the dissipated energy increases with the amplitude of loading displacement during the first five loading stages. During the fatigue loading phase, the energy dissipated by both specimens slightly decreases with the increase in the number of loading cycles. This is mainly due to a certain degree of strength degradation of BRB under fatigue cyclic loading. However, the cumulative hysteretic energy dissipation of both specimens continues to show positive growth with the increase in the number of loading cycles. Overall, the single-cycle and cumulative hysteretic energy dissipation of specimen BRB-S exceed those of specimen

BRB-L, which also indicates that in the same structure, the shorter BRB exhibits higher energy dissipation efficiency and more fully utilizes its energy dissipation capacity.

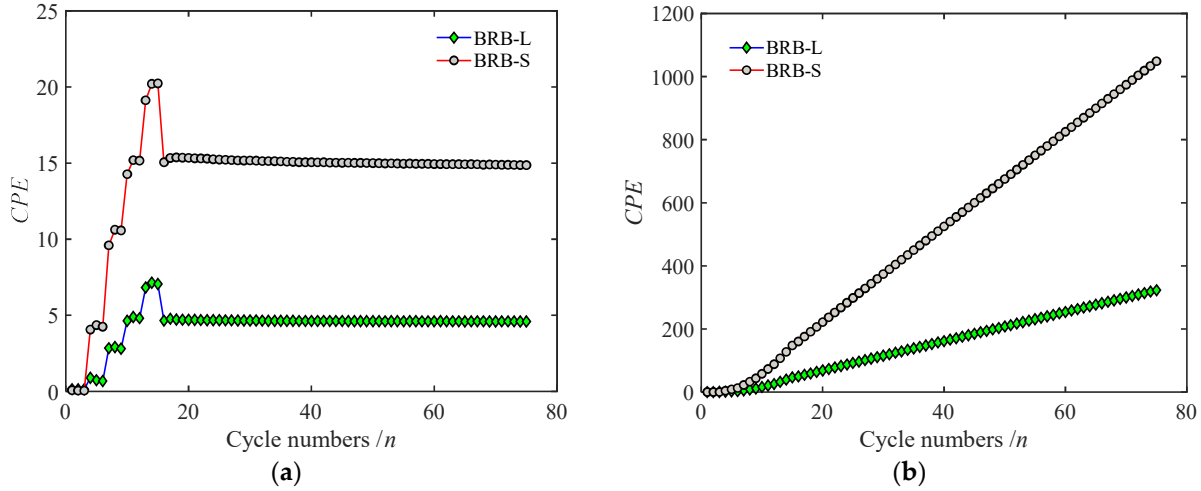


Figure 16. Energy dissipation capacity: (**a**) single-loop hysteretic energy dissipation coefficient; (**b**) cumulative hysteretic energy dissipation coefficient.

3.8. Low-Cycle Fatigue Performance

Figure 17 illustrates the low-cycle fatigue curves for specimens BRB-L and BRB-S under a loading displacement amplitude of $1.0\Delta_b$. It can be observed from the figure that neither specimen exhibited fracture failure during the 60-cycle fatigue loading process. Additionally, the hysteresis loops for each cycle showed a high degree of overlap, with no significant signs of strength or stiffness degradation. This indicates that the BRB exhibits relatively stable hysteretic energy dissipation capacity and good fatigue performance.

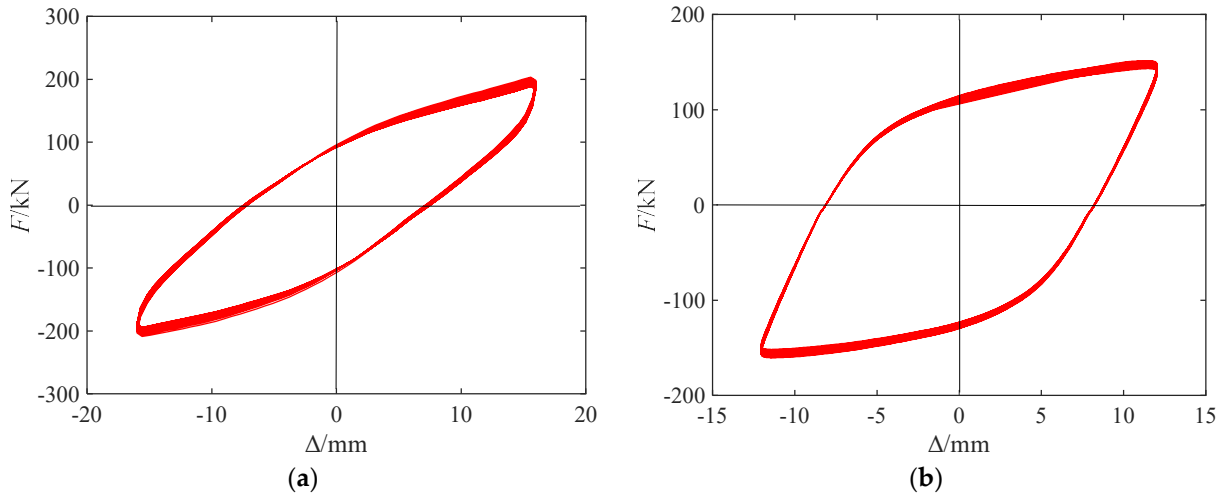


Figure 17. BRB low-cycle fatigue curve: (**a**) BRB-L; (**b**) BRB-S.

The JGJ 297-2013 [5] "Technical Specification for Energy Dissipation and Seismic Reduction of Buildings" clearly stipulates the performance parameters required for metal dampers under fatigue loading. It requires that the fatigue index parameters γ_{p1}, γ_{p2}, γ_{p3}, γ_{p4}, $\gamma_{\Delta1}$, $\gamma_{\Delta2}$, and γ_A of the damper under fatigue loading should remain within the range of 0.85 to 1.15. These parameters represent the ratio of the maximum and minimum damping forces on each hysteresis loop, the maximum and minimum damping forces at zero displacement, the maximum and minimum displacement at zero load, and the area of the hysteresis loop to the corresponding average values of all hysteresis loops [36],

respectively. Figure 18 illustrates the distribution of fatigue index parameters for specimens BRB-L and BRB-S under fatigue loading. It is evident that the fatigue index parameters for both specimens meet the requirements of the JGJ 297-2013 standard, indicating that both specimens exhibit good and stable fatigue performance. For specimen BRB-L under fatigue loading, the maximum and minimum values of parameters γ_{p1}, γ_{p2}, γ_{p3}, γ_{p4}, $\gamma_{\Delta1}$, $\gamma_{\Delta2}$, and γ_A are 1.053 and 0.976, 1.054 and 0.981, 1.031 and 0.987, 1.011 and 0.99, 1.022 and 0.965, 1.018 and 0.973, 1.029 and 0.988, respectively. For specimen BRB-S, the maximum and minimum values are 1.051 and 0.984, 1.023 and 0.983, 1.024 and 0.988, 1.023 and 0.986, 1.003 and 0.995, 1.005 and 0.994, 1.022 and 0.986, respectively. Overall, the fatigue index parameters γ_{p1}, γ_{p2}, γ_{p3}, γ_{p4}, $\gamma_{\Delta1}$, $\gamma_{\Delta2}$, and γ_A show a decreasing trend with an increasing number of loading cycles, while the fatigue parameters $\gamma_{\Delta1}$ and $\gamma_{\Delta2}$ show an increasing trend, indicating a certain degree of strength and stiffness degradation in both specimens. Furthermore, it can be observed from Figure 18 that the deviation of the fatigue index parameters from the average values for specimen BRB-S is smaller compared to specimen BRB-L, indicating that the fatigue performance of specimen BRB-S is more stable than that of specimen BRB-L.

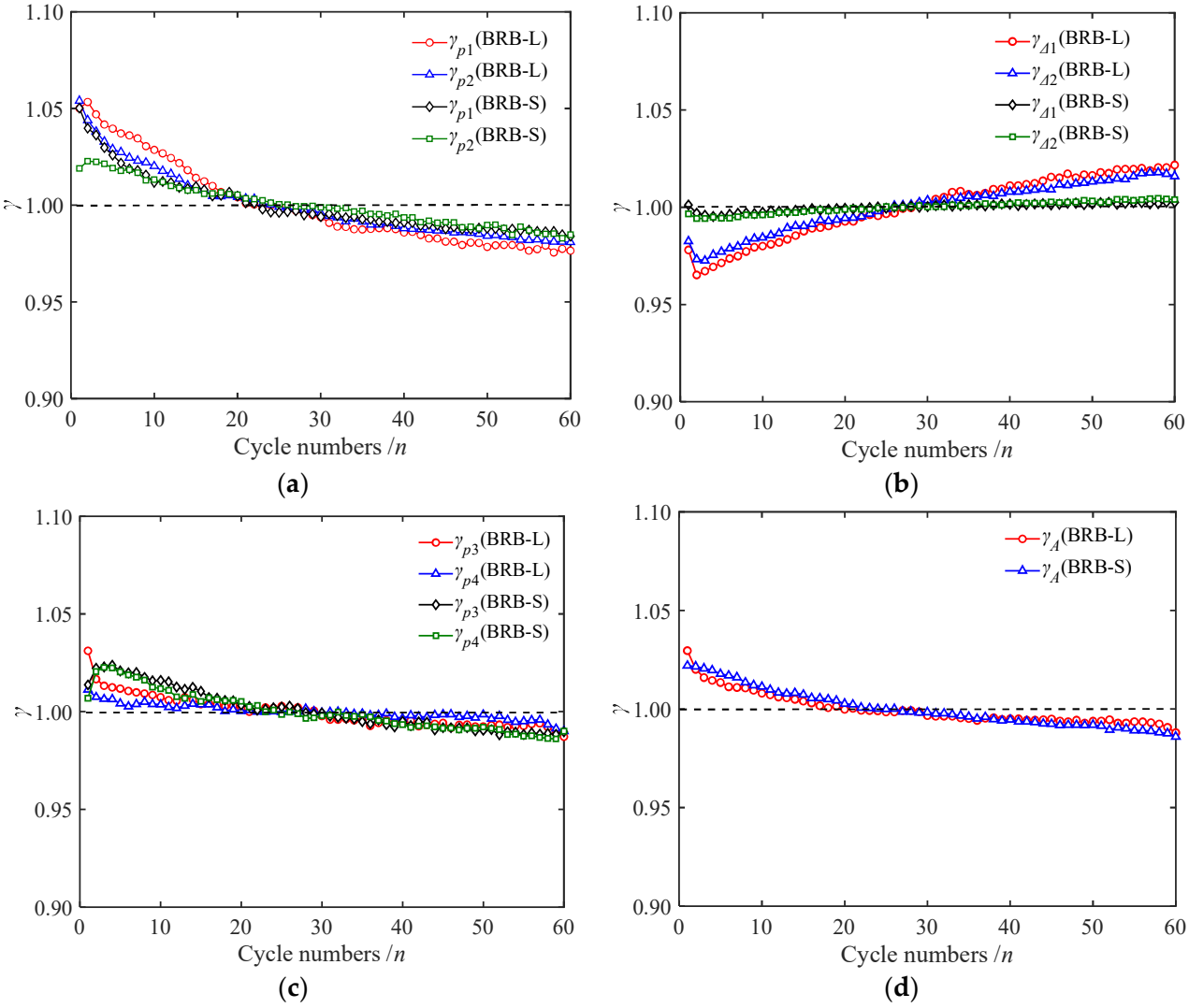


Figure 18. Fatigue performance parameters: (**a**) maximum and minimum damping force ratio; (**b**) ratio of maximum to minimum displacements at zero load; (**c**) ratio of maximum to minimum damping forces at zero displacement; (**d**) ratio of hysteresis loop areas.

4. Conclusions

This study addresses the differences in seismic performance of BRBs with significant length variations and examines how the length factor influences the energy dissipation efficiency of BRBs within the same structure. Based on a real engineering project, two BRBs with lengths of 8.5 m and 3 m were designed and subjected to low-cycle reciprocating load performance tests. This study conducted a comparative analysis of performance indicators such as hysteretic energy dissipation capacity, tension–compression imbalance coefficient, cumulative plastic deformation capacity, and low-cycle fatigue life. The findings of this research are expected to provide valuable insights for the rational selection of different lengths of BRBs in practical engineering projects and to offer preliminary guidance on the energy dissipation efficiency of BRBs of varying lengths within structures. The specific research conclusions are as follows:

(1) Both specimens BRB-L and BRB-S exhibited excellent hysteretic energy dissipation capabilities, with the skeleton curves displaying distinct bilinear characteristics. No fracture failure was observed during 60 cycles of fatigue loading. Under cyclic loading based on the design displacement, the equivalent viscous damping ratios, cumulative hysteretic energy dissipation coefficients, and cumulative plastic deformation coefficients for BRB-L and BRB-S were 26% and 39.3%, 323 and 1049, 1891 and 2146, respectively, indicating that BRB-S has a more efficient energy dissipation and damping effect.

(2) The maximum imbalance coefficients of tensile and compressive bearing capacity for BRB-L and BRB-S were 1.068 and 1.003, respectively, with the former being greater than the latter. This suggests that the length of the brace is a significant factor affecting the imbalance coefficient of BRB's tensile and compressive bearing capacity, and the longer the brace length, the larger this coefficient becomes.

(3) All fatigue performance indicators of specimens BRB-L and BRB-S met the requirements of standard JGJ 297-2013. Under fatigue loading, the maximum and minimum values of parameters γ_{p1}, γ_{p2}, γ_{p3}, γ_{p4}, $\gamma_{\Delta 1}$, $\gamma_{\Delta 2}$, and γ_A for BRB-L were 1.053 and 0.976, 1.054 and 0.981, 1.031 and 0.987, 1.011 and 0.99, 1.022 and 0.965, 1.018 and 0.973, 1.029 and 0.988, respectively. For BRB-S, the maximum and minimum values were 1.051 and 0.984, 1.023 and 0.983, 1.024 and 0.988, 1.023 and 0.986, 1.003 and 0.995, 1.005 and 0.994, 1.022 and 0.986, respectively. The parameters of BRB-S deviated less from the average values, indicating more stable low-cycle fatigue performance.

(4) Within the same structure, shorter BRB lengths and larger design displacements result in higher energy dissipation efficiency and more effective utilization of energy dissipation capacity.

Author Contributions: Conceptualization, K.W. and G.W.; methodology, C.L.; software, W.Y.; validation, W.Y., X.L. and L.Z.; formal analysis, K.W.; investigation, K.W.; resources, G.W.; data curation, L.Z.; writing—original draft preparation, K.W.; writing—review and editing, G.W.; visualization, C.L.; supervision, W.Y.; project administration, X.L.; funding acquisition, L.Z. All authors have read and agreed to the published version of the manuscript.

Funding: This research was funded by Yunnan Provincial Local Universities Joint Special Project (Grant No. 202101BA070001-176, 202101BA070001-159), Scientific Research Fund Project of the Yunnan Provincial Department of Education (Grant No. 2025J1150), Project of the Scientific Research Characteristic Team for Research and Application of Seismic Isolation and Mitigation Technologies in High-Intensity Areas (No. XJ20230036).

Data Availability Statement: All the data utilized in the research have been fully presented in the paper. No additional data have been employed.

Conflicts of Interest: The authors declare no conflicts of interest.

References

1. Iwata, M. Applications-design of Buckling Restrained Braces in Japan. In Proceedings of the 13th World Conference on Earthquake Engineering, Vancouver, BC, Canada, 1–6 August 2004.
2. Huang, H.; Chen, Z.; Zhao, M.; Wang, B.; Ye, Y. Seismic Performance of Frame with Middle Partially Encased Composite Brace and Steel-Hollow Core Partially Encased Composite Spliced Frame Beam. *J. Build. Eng.* **2024**, *95*, 110226. [CrossRef]
3. Ali, A.; Zhang, C.; Bibi, T.; Sun, L. Experimental Investigation of Sliding-Based Isolation System with Re-Centering Functions for Seismic Protection of Masonry Structures. *Structures* **2024**, *60*, 105871. [CrossRef]
4. Li, W.; Dong, J.; Qu, H.; Wang, L.; Zhao, K. Local Buckling Development of H-Section Steel Core of Buckling-Restrained Brace. *Buildings* **2022**, *12*, 227. [CrossRef]
5. *JGJ 297-2013*; Chinese Standard, Technical Specification for Seismic Energy Dissipation of Buildings. China Architecture & Building Press: Beijing, China, 2013.
6. Zhou, Y.; Shao, H.; Cao, Y.; Lui, E.M. Application of Buckling-Restrained Braces to Earthquake-Resistant Design of Buildings: A Review. *Eng. Struct.* **2021**, *246*, 112991. [CrossRef]
7. Ullah, R.; Vafaei, M.; Alih, S.C.; Waheed, A. A Review of Buckling-Restrained Braced Frames for Seismic Protection of Structures. *Phys. Chem. Earth* **2022**, *128*, 103203. [CrossRef]
8. Pandikkadavath, M.S.; Sahoo, D.R. Analytical Investigation on Cyclic Response of Buckling-restrained Braces with Short Yielding Core Segments. *Int. J. Steel Struct.* **2016**, *16*, 1273–1285. [CrossRef]
9. Pandikkadavath, M.S.; Sahoo, D.R. Cyclic Testing of Short-Length Buckling-Restrained Braces with Detachable Casings. *Earthq. Struct.* **2016**, *10*, 699–716. [CrossRef]
10. Gao, C.; Chen, X.; Wang, X.; Li, G. Analysis of Hysteresis Behavior of Short-Yielding-Section Buckling-Restrained Brace. *J. Xi'an Univ. Arch. Technol. Nat. Sci. Ed.* **2023**, *55*, 819–826.
11. Sitler, B.; Takeuchi, T. Higher-Mode Buckling and Friction in Long and Large Scale Buckling Restrained Braces. *Struct. Des. Tall Spec. Build.* **2020**, *30*, e1812. [CrossRef]
12. Mirtaheri, M.; Gheidi, A.; Zandi, A.P.; Alanjari, P.; Samani, H.R. Experimental Optimization Studies on Steel Core Lengths in Buckling Restrained Braces. *J. Constr. Steel Res.* **2011**, *67*, 1244–1253. [CrossRef]
13. Kazemi, F.; Asgarkhani, N.; Lasowicz, N.; Jankowski, R. Development and Experimental Validation of a Novel Double-Stage Yield Steel Slit Damper-Buckling Restrained Brace. *Eng. Struct.* **2024**, *315*, 118427. [CrossRef]
14. Xiong, C.; Cao, Y.; Wang, T.; Xie, L.; Wu, D. Experimental and Numerical Studies of a Core Plate Repairable Double-Stage Yield Buckling-Restrained Brace. *J. Constr. Steel Res.* **2024**, *223*, 109006. [CrossRef]
15. Sun, J.; Pan, P.; Wang, H. Development and Experimental Validation of an Assembled Steel Double-Stage Yield Buckling Restrained Brace. *J. Constr. Steel Res.* **2018**, *145*, 330–340. [CrossRef]
16. Wu, C.; Zhang, Q.; Gong, C.; Li, D.; Zhang, Y.; Chen, Z. A Double-Stage Buckling Restrained Brace with Progressive Failure Pattern: Experimental Verification and Numerical Calibration. *Structures* **2024**, *62*, 106242. [CrossRef]
17. Guo, Y.L.; Liu, J.B.; Cai, Y.Y.; Deng, K. Energy Dissipation and Buckling-Restrained Braces of Structures. *Build. Struct.* **2005**, *35*, 18–23. (In Chinese)
18. Zhou, Y.; Zhong, G.Q.; Chen, Q.X.; Gong, C. Experimental Study on the Performance of Assembled Buckling-Restrained Braces with Different Steel Plate Structures. *China Civ. Eng. J.* **2017**, *50*, 9–17. (In Chinese)
19. Jia, M.M.; Li, F.H.; Lu, B.B. Experimental Study on Assembled Buckling-Restrained Braces with Carbon Fiber Wrapping Constraint. *J. Harbin Inst. Technol.* **2016**, *48*, 98–104. (In Chinese)
20. Lu, J.K.; Li, Y.Y.; Ding, Y. Experimental Study on Buckling-Restrained Braces with Variable Thickness Steel Plate Inner Core. *World Earthq. Eng.* **2020**, *36*, 90–95. (In Chinese)
21. Wu, A.C.; Lin, P.C.; Tsai, K.C. High-Mode Buckling Responses of Buckling-Restrained Brace Core Plates. *Earthq. Eng. Struct. Dyn.* **2014**, *43*, 375–393. [CrossRef]
22. Fujita, M.; Nakamura, M.; Awazu, K.; Iwata, M. Effects of the Clearance between the Core Plate and Restraining Part on the Structural Performance of the Buckling-Restrained Brace Using Steel Mortar Planks. *Steel Constr.* **2022**, *15*, 1–12. [CrossRef]
23. GB/T 228.1-2010. Chinese Standard, Metallic Materials—Tensile Testing—Part 1: Method of Test at Room Temperature. General Administration of Quality Supervision: Beijing, China, 2010.
24. *DBJ 53/T-125-2021*; Chinese Standard, Technical Specification for Application of Seismic Energy Dissipation in Buildings. Department of Housing and Urban-Rural Development of Yunnan Province: Kunming, China, 2021.
25. Dehghani, M.; Tremblay, R. Design and Full-Scale Experimental Evaluation of a Seismically Endurant Steel Buckling-Restrained Brace System. *Earthq. Eng. Struct. Dyn.* **2018**, *47*, 105–129. [CrossRef]
26. Wang, C.L.; Usami, T.; Funayama, J. Improving Low-Cycle Fatigue Performance of High-Performance Buckling-Restrained Braces by Toe-Finished Method. *J. Earthq. Eng.* **2012**, *16*, 1248–1268. [CrossRef]
27. Wu, K.; Tao, Z.; Pan, W.; Bai, Y. A Local Buckling Design Method of All-Steel Buckling-Restrained Brace Considering the Effect of Friction. *J. Vib. Shock.* **2020**, *39*, 240–252.

28. *ANSI/AISC 341-16*; Seismic Provisions for Structural Steel Buildings. American Institute of Steel Construction (AISC): Chicago, IL, USA, 2016.
29. *JGJ 99-2015*; Chinese Standard, Technical Specification for Steel Structure of Tall Building. China Architecture & Building Press: Beijing, China, 2015.
30. Genna, F.; Gelfi, P. Analysis of the Lateral Thrust in Bolted Steel Buckling-Restrained Braces. *I Exp. Numer. Results. J. Struct. Eng.* **2012**, *138*, 1231–1243.
31. Chen, L.; Wang, D.S.; Sun, Z.G.; Qian, H. Experimental Study on the Seismic Performance of Assembled Perforated Stainless Steel Buckling-Restrained Braces. *Eng. Mech.* **2024**, *41*, 226–238. (In Chinese)
32. Lin, P.C.; Tsai, K.C.; Chang, C.A.; Hsiao, Y.; Wu, A. Seismic Design and Testing of Buckling-Restrained Braces with a Thin Profile. *Earthq. Eng. Struct. Dyn.* **2016**, *45*, 339–358. [CrossRef]
33. *JGJ/T 101-2015*; Chinese Standard, Technical Specification for Seismic Energy Dissipation of Buildings. China Architecture & Building Press: Beijing, China, 2015.
34. Yang, Z.; Liu, D.; Zhou, J.; Zhang, L.; Liao, W. Seismic Vulnerability Assessment of the Cliff-Attached Buildings Equipped with Energy Dissipation Devices Under Obliquely Incident Seismic Waves. *Buildings.* **2024**, *14*, 3488. [CrossRef]
35. Yang, L.; Wei, X.; Shi, G.; Xiao, S.Y. Experimental Study on the Energy Dissipation Performance of LY315 Steel Buckling-Restrained Braces. *Eng. Mech.* **2019**, *36*, 200–206. (In Chinese)
36. Wang, M.; Tong, Y. Experimental study on seismic performance of assembled buckling-restrained brace with low yield point steel. *Thin-Walled Struct.* **2024**, *205*, 112474. [CrossRef]

Disclaimer/Publisher's Note: The statements, opinions and data contained in all publications are solely those of the individual author(s) and contributor(s) and not of MDPI and/or the editor(s). MDPI and/or the editor(s) disclaim responsibility for any injury to people or property resulting from any ideas, methods, instructions or products referred to in the content.